Transient Stability Analysis and Modelling of Systems with Grid-Forming Converters and Synchronous Generators

Xianxian Zhao[1], Xavier Kestelyn[2], Damian Flynn[1]*

[1]*School of Electrical and Electronic Engineering, University College Dublin, Belfield, Dublin, Ireland*
[2]*ULR 2697–L2EP, Centrale Lille, Junia ISEN Lille, Arts et Metiers Institute of Technology, University of Lille, France*
**xianxian.zhao@ucd.ie*

Keywords: Grid-forming converter (GFM), synchronous generator (SG), transient stability, model order reduction, electromagnetic (EMT) simulation.

Abstract

The transient stability of a power system with both grid-forming converters (GFMs) and synchronous generators (SGs) under large faults is rarely reported. This paper finds out that even when a SG and GFM have the same frequency during a fault by setting the same inertia and damping coefficient for both, due to the impact of the dynamics of the SG field and amortisseur flux linkage, a parallel connected GFM with low capacity ratio between the GFM and SG outputs negative postfault active power. In other words, the GFM becomes synchronization unstable according to traditional definition. Since normally a GFM has much larger damping (to have strong robustness during small and large disturbances), this negative active power is even lower and lasts longer in practical cases. When conducting transient stability analysis, existing methods usually model a GFM in the same form as the classic SG model, and did not provide theoretical analysis. To simplify analysis and facilitate control design under large disturbances, this paper adopts a modal analysis-based model order reduction technique and finds out that while a GFM can be modelled as the classic form together with the virtual impedance current limiting control, the interacted SGs should not be modelled in the classic form, because the SG field and amortisseur flux linkage should also be included. Finally, this paper finds that for systems with only GFMs as voltage sources, reserving only the dynamics of the voltage angle control loop of GFMs is precise enough for representing the system low-frequency oscillations phenomenon.

1 Introduction

As part of efforts to reduce carbon emissions and combat climate change, many power systems are rapidly transitioning towards converter-based variable renewable generation, mainly from wind and photovoltaic sources [1]. Existing power converters are mostly controlled as "grid-following", using a phase-locked loop (PLL) to synchronize the voltage angle at the point of common coupling, so that they can realise active and reactive decoupling control and precisely follow the power setpoints [2]. However, as grid-following converters (GFLs) rely on following grid voltage, at higher GFL shares in terms of capacity, with synchronous generation being gradually displaced, they can no longer remain synchronized and thus are unable to maintain controlled and stable outputs [3, 4].

Consequently, the "grid-forming" concept has been proposed, such that grid-forming converters (GFMs) independently create their own internal voltage angle using an external input signal such as active power reference. One of the simplest GFMs is mimicked ideal AC voltage sources by fixing their frequency at the rated one. Thus, GFMs can maintain their voltage angle and provide an immediate response to voltage and frequency disturbances, and naturally, inherent the abilities of synchronous machines, such as inertial response, offering blackstart capability, and providing a voltage reference for GFL converters. Consequently, GFMs are often seen as a replacement for synchronous machines in future power grids.

Due to the fast and flexible controllability of voltage source converters, GFMs can exhibit very good dynamic and steady-state performances under small disturbances, if their parameters are properly tuned using small-signal analysis. However, under large transient disturbances, such as faults on transmission facilities, GFMs can easily go into current saturation, due to much lower overcurrent capability of voltage source converters compared to synchronous generators (SGs) (while a SG can provide six times its rate current, a VSC can only cope with two times its rated current in one millisecond [5]). During such transients, grid-forming abilities are greatly limited or even lost. Small-signal models are not sufficient to analyse the response to large disturbances, and non-linear models which are valid for large signals and control switching are required. In addition, effective analytical tools to facilitate the design the control and tuning of the parameters under large disturbances are still not mature, especially in realistic cases where systems may consist of a mix of GFM, GFL and SGs.

Transient stability of systems with GFMs connecting to infinite bus [6-11], or with only GFMs as voltage sources [12, 13] under severe faults has been extensively studied, while systems with both GFMs and SGs are rarely reported. In [14], transient stability of a small isolated microgrid with an SG and virtual synchronous generator (VSG) and with two equal VSGs are compared, and it is shown that the paralleled SG-VSG system is more prone to transient instability due to the differences between their speed governors. However, the work in this paper will show that a GFM-only grid is not

necessarily more stable than a mixed grid, if the GFMs employ diverse parameter settings for the voltage angle control. [15] proposed that the virtual angular speed of the GFMs is frozen at a value equal to the weighted mean of the SMs rotor speeds under faults, so that the change of the relative angle between the GFMs and SGs is minimized and the transient stability of the SG-GFM system is improved. However, as demonstrated in this paper, the transient stability is not only impacted by the relative angle between them, but also by the rotor field and amortisseur of the SGs.

This paper makes the following contributions to the modelling and analysis of the transient stability of systems consisting of GFMs and SGs:

- The transient stability of systems with both GFMs and SGs under large faults is studied. It finds out that even when SG and GFM have the same rotor speed during a fault by setting the same inertia and damping coefficient for both, due to the dynamics of the SG rotor field flux and amortisseur flux, under certain conditions a small GFM by capacity can output negative postfault active power. This means the GFM is unstable according to traditional definition. The negative active power output becomes lower and lasts longer in real applications because typical GFMs have much larger damping coefficients.
- To simplify analysis and control design for large events like faults, existing methods typically model a GFM in the same form as the classic SG model [6-8, 12], or plus a 1st order differential [9, 10] or 0th algebraic equation for the reactive power and voltage amplitude droop control [11], without providing theoretical analysis. This paper adopts a modal analysis-based model order reduction technique that optimizes the reduced number of a system's state variables depending on the observed variables and considered events, and finds out that while a GFM can be modelled as the classic form along with the virtual impedance current limiting control, the nearby SG should be modelled not only with the dynamics of the active power and angle but also with that of the rotor field and amortisseur flux linkage.
- This paper finds that for systems with only GFMs as voltage sources, reserving only the state variables of the voltage angle and angular speed of GFMs is enough for representing the low-frequency oscillations phenomenon of the system.

Section 2 presents the full electromagnetic model of a typical GFM and its equivalent inertia and damping. Time-domain electromagnetic (EMT) simulations of systems with both GFMs and SG are conducted in Section 3 to show the low and negative postfault active power output of a GFM under faults. In Section 4, the MOR technique in [16] is reviewed and implemented, to deduce the most relevant state variables of the system that induces such negative active power for GFMs. In Section 5, the transient stability of systems with only GFMs under divergent inertia and damping settings are investigated. Section 6 presents the conclusion.

2. Grid-Forming Converter

The full EMT model of the classic droop control-based grid-forming converter, and its equivalent damping and inertia are described in this section.

2.1 Grid-Forming Converter General Structure

GFMs are designed to act as voltage sources instead of current sources (which is the case for grid-following converters), and therefore can replace synchronous machines (which create the voltage in today's power systems).

The physical structure of a droop control based GFM and its control studied in this paper is shown in Fig. 1. It's a classical structure that can be found in [17, 18]. The GFM is made of a DC/AC converter (here DC voltage source is assumed constant, and DC/AC converter is assumed to be ideal), an RLC filter and transformer, and the control part consists of P/f voltage angle control loop, outer voltage amplitude control loop, and inner cascaded voltage and current proportional-integral (PI) control loops.

Note that Fig. 1 can be thought as a representative GFM, because the dynamic characteristics relevant in this paper are mainly decided by the outer voltage amplitude and angle control, and despite the differences between droop control, VSG, and virtual oscillator, all those methods have a similar property of behaving a voltage source behind an impedance, which allows GFMs offer blackstart capability and maintain their voltage angle and provide an immediate response to voltage and frequency disturbances.

In the following the difference between an algebraic and differential variable is that a differential variable is expressed with a differential term d/dt.

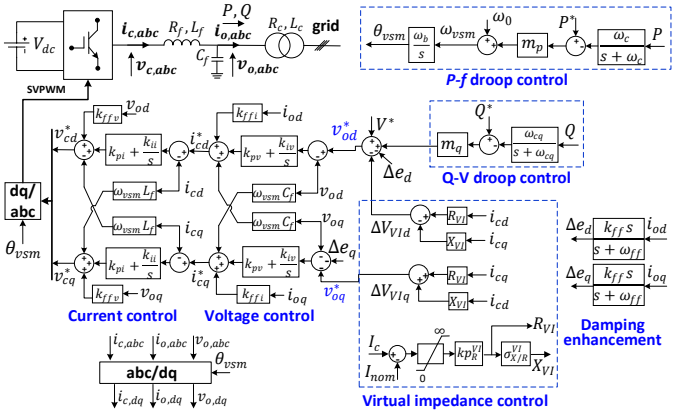

Fig. 1 Grid-forming converter with a LCL filter based on droop control, with virtual impedance current limiting control and a damping enhancement block.

2.2 Grid-Forming Converter Control Part Modelling

The equations of the P/f droop control are given in (1)(2), where P, p_m, ω_{vsm} and δ_{vsm} are the active power injected by the converter, the measure of this power, the virtual angular speed generated by the P/f droop control, and the angle of the converter, respectively.

$$P = v_{od}i_{od} + v_{oq}i_{oq}, \tag{1a}$$

$$\frac{dp_m}{dt} + \omega_c p_m = \omega_c P, \tag{1b}$$

$$\omega_{vsm} = \omega_0 + m_p(P^* - p_m), \tag{2a}$$

$$\frac{1}{\omega_b}\frac{d\delta_{vsm}}{dt} = \omega_{vsm} - \omega_0, \tag{2b}$$

The equations of the reactive power and voltage amplitude, Q/V, droop control, along with a damping enhancement control, and virtual impedance (VI) current limiting control, are given in (3)-(6), where Q and q_m are the reactive power injected by the converter and the measure of this power, v_{od}^* and v_{oq}^* are d- and q-axis voltage reference for the voltage PI controller, M_{ADd} and M_{ADq} are the states for the damping enhancement control, Δv_{VId} and Δv_{VIq}, R_{VI} and X_{VI} are the output voltage and virtual resistor and inductance of the VI current control, and i_c is the converter's current. The principle of the VI current limiting control is that an emulated impedance is added to the $R_f L_f$ filter once the GFM current is larger than I_{nom}, so that the converter's current is limited.

$$Q = v_{oq} i_{od} - v_{od} i_{oq}, \tag{3a}$$

$$\frac{dq_m}{dt} + \omega_{fq} q_m = \omega_{fq} Q. \tag{3b}$$

$$v_{od}^* = V^* + m_q(Q^* - q_m) + \left(M_{ADd} - k_{ff} i_{od}\right) - \Delta v_{VId}, \tag{4a}$$

$$v_{oq}^* = \left(M_{ADq} - k_{ff} i_{oq}\right) - \Delta v_{VIq}. \tag{4b}$$

$$\frac{dM_{ADd}}{dt} = \omega_{ff}\left(k_{ff} i_{od} - M_{ADd}\right), \tag{5a}$$

$$\frac{dM_{ADq}}{dt} = \omega_{ff}\left(k_{ff} i_{oq} - M_{ADq}\right). \tag{5b}$$

$$\Delta v_{VId} = R_{VI} i_{cd} - X_{VI} i_{cq}, \tag{6a}$$

$$\Delta v_{VIq} = R_{VI} i_{cq} + X_{VI} i_{cd}, \tag{6b}$$

$$R_{VI} = k_{pR}^{VI} \max(0, i_c - I_{nom}), \tag{6c}$$

$$X_{VI} = \sigma_{X/R}^{VI} R_{VI}, \tag{6d}$$

$$i_c = \sqrt{i_{cd}^2 + i_{cq}^2}. \tag{6e}$$

The equations for the PI control loop of the output voltage across the capacitor C_f are given in (7)(8), where ξ_d and ξ_q are the d- and q-axis states for the integrator, and i_{cd}^* and i_{cq}^* are the current reference for the inner current control loop.

$$\frac{d\xi_d}{dt} = k_{iv}(v_{od}^* - v_{od}), \tag{7a}$$

$$\frac{d\xi_q}{dt} = k_{iv}\left(v_{oq}^* - v_{oq}\right). \tag{7b}$$

$$i_{cd}^* = k_{ffi} i_{od} + k_{pv}(v_{od}^* - v_{od}) - \omega_{vsm} C_f v_{oq} + \xi_d, \tag{8a}$$

$$i_{cq}^* = k_{ffi} i_{oq} + k_{pv}\left(v_{oq}^* - v_{oq}\right) + \omega_{vsm} C_f v_{od} + \xi_q. \tag{8b}$$

The equations for the PI control loop of the converter current through the R_f, L_f filter are given in (9)(10), where σ_d and σ_q are the d- and q-axis states for the integrator, v_{cd}^* and v_{cq}^* are d- and q-axis voltage reference of the DC/AC converter.

$$\frac{d\sigma_d}{dt} = k_{ii}(i_{cd}^* - i_{cd}), \tag{9a}$$

$$\frac{d\sigma_q}{dt} = k_{ii}\left(i_{cq}^* - i_{cq}\right). \tag{9b}$$

$$v_{cd}^* = k_{ffv} v_{od} + k_{pi}(i_{cd}^* - i_{cd}) - \omega_{vsm} L_f i_{cq} + \sigma_d, \tag{10a}$$

$$v_{cq}^* = k_{ffv} v_{oq} + k_{pi}\left(i_{cq}^* - i_{cq}\right) + \omega_{vsm} L_f i_{cd} + \sigma_q. \tag{10b}$$

2.3 Grid-Forming Converter Physical Part Modelling

The equations that model the RL filter, C filter and DC/AC converter are given in (11), (12) and (13), respectively. These equations are given in a DQ0 reference frame of the angular frequency ω_{vsm} given by the P/f external control loop.

$$\frac{L_f}{\omega_b}\frac{di_{cd}}{dt} = v_{cd} - v_{od} - R_f i_{cd} + \omega_{vsm} L_f i_{cq}, \tag{11a}$$

$$\frac{L_f}{\omega_b}\frac{di_{cq}}{dt} = v_{cq} - v_{oq} - R_f i_{cq} - \omega_{vsm} L_f i_{cd}. \tag{11b}$$

$$\frac{C_f}{\omega_b}\frac{dv_{od}}{dt} = i_{cd} - i_{od} + \omega_{vsm} C_f v_{oq}, \tag{12a}$$

$$\frac{C_f}{\omega_b}\frac{dv_{oq}}{dt} = i_{cq} - i_{oq} - \omega_{vsm} C_f v_{od}. \tag{12b}$$

$$v_{cd}^* = v_{cd}, \tag{13a}$$

$$v_{cq}^* = v_{cq}. \tag{13b}$$

(13) indicates that an ideal DC/AC converter is assumed.

The output voltage and current in (1)(2) need to be converted to the common DQ0 reference frame rotating at a frequency of ω, with base capacity of 100 MVA. Given a converter capacity of S_b, the conversions are presented as (14)(15).

$$\frac{100}{S_b}\begin{bmatrix} i_{od} \\ i_{oq} \end{bmatrix} = \begin{bmatrix} \cos(\delta_{vsm}) & -\sin(\delta_{vsm}) \\ \sin(\delta_{vsm}) & \cos(\delta_{vsm}) \end{bmatrix}\begin{bmatrix} i_{od}^g \\ i_{oq}^g \end{bmatrix}, \tag{14}$$

$$\begin{bmatrix} v_{od} \\ v_{oq} \end{bmatrix} = \begin{bmatrix} \cos(\delta_{vsm}) & -\sin(\delta_{vsm}) \\ \sin(\delta_{vsm}) & \cos(\delta_{vsm}) \end{bmatrix}\begin{bmatrix} v_{od}^g \\ v_{oq}^g \end{bmatrix}. \tag{15}$$

The modelling for the output transformer (i.e. the $R_c L_c$ filter shown in Fig. 2) is the same as (11), and hence not repeated.

2.4 GFM Equivalent Inertia and Damping

The P/f droop control described in (1) and (2) can be re-written as (16).

$$\omega_{vsm} = \frac{1}{\frac{1}{m_p \omega_c} s + \frac{1}{m_p}}(P^* - P) + \omega_0. \tag{16}$$

For a SG, the rotor speed can be written as (17).

$$\omega_r - \omega_0 = \frac{1}{2Hs + K}(P^* - P). \tag{17}$$

Therefore, the equivalent damping and inertia of the GFM can be described as (18)(19).

$$K_{eq} = \frac{1}{m_p}, \tag{18}$$

$$H_{eq} = \frac{1}{2 m_p \omega_c}. \tag{19}$$

3. Grid-Forming Converters Negative Active Power Output with Connection to SGs

3.1 System Short-Circuit Response With A Typical GFM Connecting to a SG under Very Different Damping

In this section, detailed full nonlinear EMT simulations of Fig. 2 under 3-phase bolted faults are studied, to investigate the transient stability of systems with a mix of GFMs and SGs as voltage sources.

The physical modelling and parameters of the SG are the same as that in Example 12.6 in [19]. The SG is equipped with a high gain thyristor excitor. To simplify analysis, the SG is not equipped with power system stabilizer (PSS) and governor in the following cases. However, when they are included in a SG, simulation results (not shown here) show that their impacts on the active power output of the connected GFM with small GFM and SG capacity ratio should be included, and their models can be simplified with fewer low-pass transfer functions with the limitations. The model of the

SG with the output transformer and RL-transmission line is 11 order in total (rotor angle, rotor angular speed, d- and q-axis stator flux linkage, field rotor flux linkage, 1 d-axis and 2 q-axis rotor amortisseur flux linkage, 1 order for the low-pass filter for the terminal voltage in the excitor, and 2 order for the transformer and RL-line).

The GFM full EMT model plus its output transformer and RL-transmission line is 15 order in total, which is presented in Section 2. Its physical and control parameters are the same as [20], which are shown in Table 1. Note that virtual impedance current limiting control is activated when the GFM current is ≥1 pu and the current limit is 1.2 pu.

The power setpoints for each generator are based on its own pu system associated to its S_b and V_b. For the grid, $S_b = 100$ MVA, V_b is the same in the whole system. The capacity of the G1 is 100 MVA, and of the G2 is 900 MVA. The active and reactive power and voltage setpoints for both generators are the same, which are 0.5 pu, 0 pu, and 1 pu. To generate the same voltage drop across the two lines, the length of Line 1 is 9 times that of Line 2, with resistance and inductance of 0.0018 pu and 0.018 pu, and 0.0002 pu and 0.002 pu, respectively. The resistance and inductance of the two transformers are 0.005 pu and 0.15 pu based on each generator S_b. The resistance and inductance of the load is 0.1986 pu and -0.0169 pu, based on grid S_b. In the following each case, a bolted 3-phase fault of 250 ms is applied at the load bus at 0.15 s. The equivalent damping and inertia of the GFM are calculated based on (18)(19).

The simulations in the following are performed using Dymola software, based on Modelica language, where model details are completely transparent. The simulation time step is 0.0001 s, which is small enough for the transient stability studies in this paper.

Case 1: G1 is a GFM and G2 a SG. To ensure a robust operation under different disturbances, GFMs normally are equipped with large damping coefficient. Hence, the GFM with $m_p = 0.01$ pu, equivalent to a damping of 100 pu, is simulated in this case. Then $\omega_c = 10$ rad/s is set, to let the GFM have the same inertia as the SG of 5 s. The inertia and damping for the SG are set as $H^{SG} = 5$ s and $K_D^{SG} = 5$ pu.

The simulation results of Case 1 are shown in Fig. 3. Fig. 3(a) shows the GFM postfault active power output is very low and negative (hitting the limit -1 pu), which takes about 400 ms to reach the prefault value, but then decreases again to 0.1 pu and takes another 1 s to recover. This is synchronisation unstable according to traditional definition, which for GFMs may need to be re-defined based on practical applications.

One of the reasons for above negative GFM active power output is the reduction of the angle difference between the GFM and SG, as shown in Fig. 3(c), since the GFM has much larger damping than the SG (100 vs. 5 pu), leading to the GFM virtual angular speed being slower than the SG rotor speed during the fault, as can be seen in Fig. 3(b).

Another major reason is originated from the impacts of the dynamics of the SG rotor field and amortisseur flux linkage, which prevent the change of the rotor speed of the SG. This will be demonstrated by the following Case 2.

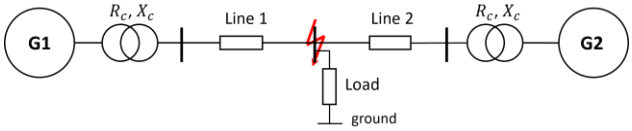

Fig. 2 A typical study system consisting of a grid-forming converter, synchronous generator, constant impedance load and RL-transmission lines.

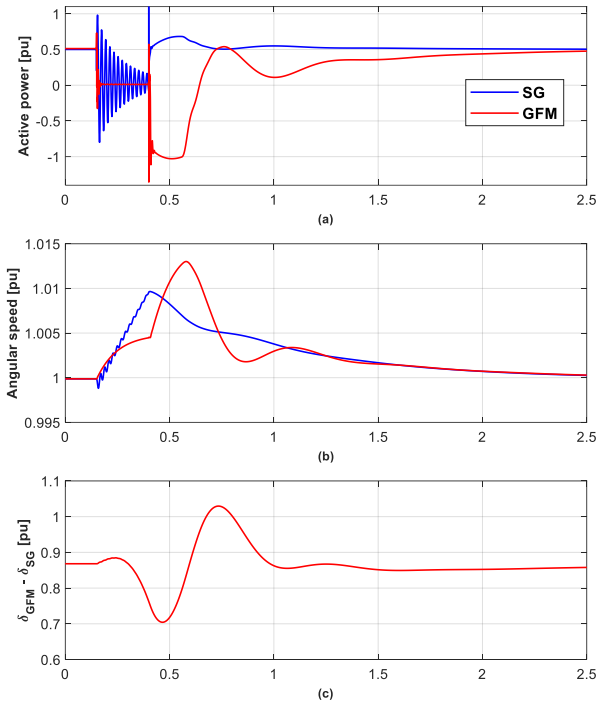

Fig. 3 The simulation results of Case 1. (a)(b) The GFM and SG active power output and (virtual) angular speeds, and (c) the voltage angle difference between the GFM and SG.

Table 1 Circuit and control parameters for droop control-based grid-forming converter

Parameters	Value (pu)
R_f, L_f, C_f	0.005, 0.15, 0.066
R_c, L_c	0.005, 0.15
$k_{pv}, k_{iv}, k_{pi}, k_{ii}$	0.52, 1.16, 0.74, 1.19
k_{ffi}, k_{ffv}	1, 1
$kp_R^{VI}, \sigma_{X/R}^{VI}$	0.67, 5
I_{nom}, I_{max}^{VI}	1, 1.2
m_p, m_q	0.02, 0.0001
ω_c, ω_{cq}	31.4 rad/s, 31.4 rad/s
ω_0, ω_b	1, 314 rad/s
k_{ff}, ω_{ff}	0.01, 16.66 rad/s

3.2 System Short-Circuit Response With A GFM Connecting to a SG with the Same Inertia and Damping

Case 2: The settings are same as Case 1, but the GFM now has the same inertia and damping as the SG, i.e. $m_p = 0.2$ pu, $\omega_c = 0.5$ rad/s. Setting the same inertia and damping for

both GFM and SG is to find out whether the phenomenon of the GFM in Case 1 outputting very low and negative active power output is only caused by the reduction of the relative voltage angle difference between the GFM and SG.

The simulation results of Case 2 are shown Fig. 4. Comparing to Fig. 3(c), Fig. 4(c) shows that the voltage angle difference between the GFM and SG is now increased at the time point of the fault clearing (at 0.4 s). However, Fig. 4(a) shows that the GFM active power is not higher than the SG at 0.4 s as expected, but is still very low and negative, reaching -0.7 pu. This illustrates that GFM active power output is also affected by the electrical dynamics in the system. On the other hand, by comparing Fig. 3(a) and Fig. 4(a), the low active power output of the GFM is seen mitigated (being higher and lasting shorter time duration). This confirms that the reduction of the angle difference between the GFM and SG indeed causes the GFM active power output low and even negative.

Noted that although the inertia and damping of the GFM and SG are the same, the virtual angular speed of the GFM is not the same, but slightly higher than that of the SG, as can be seen in Fig. 4(b). This is because the active power output of the SG is slightly higher than that of the GFM during the fault (Fig. 4(a)), since the SG is contributing much higher current and has higher output voltage than the GFM (Fig. 4(d)).

Different from Fig. 3(a), Fig. 4(a) shows that the postfault active power of the GFM has large oscillations which convergent very slowly. The eignanalysis of Cases 1 and 2 in Fig. 5 show that different from Case 1, in Case 2 appears a pair of eigenvalues which has very small damping and is close to the imaginary axis. This pair of eigenvalues is mainly participated by the states δ_{GFM} and ω_{vsm} of the GFM (the sum participation factor of both states is >90%). This explains why the (equivalent) damping for a GFM is normally set large.

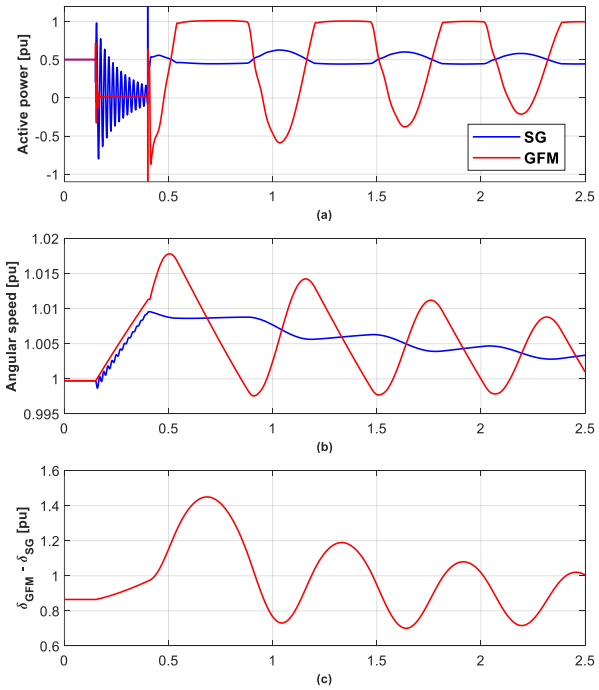

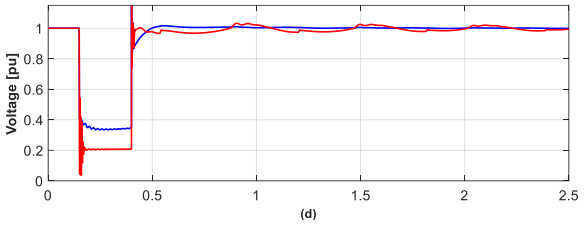

Fig. 4 The simulation results of Case 2. (a)(b) The active power output and (virtual) angular speeds of the GFM and SG, (c) the voltage angle difference between the GFM and SG, and (d) the output voltage of the GFM and SG.

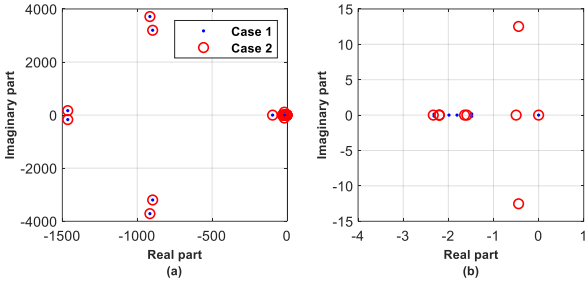

Fig. 5 (a) Eigen-analysis of Cases 1 & 2, and (b) zoom of (a).

4 Transient Stability Analysis and Modelling Simplification with Both Grid-Forming Converters and Synchronous Generators

For transient stability analysis under large disturbances such as faults, due to the strong non-linear relationship among the state variables, the modal analysis-based model order reduction technique in [16] is adopted here, in order to

- deduce which state variables of the system in Fig. 2 have the most impact on the GFM active power output, and
- reduce the number of the system state variables, in order to simplify analysis and control design.

Compared to the classical phasor approximation, this event-based state residualization approximation technique allows accurate transient simulations and at the same time an optimal reduction of the number of the system state variables depending on the observed variables, considered events and tolerated approximation error.

In the following of this section, this MOR technique is briefly introduced and then applied to the studied system, and finally time domain EMT simulations are performed to demonstrate the feasibility of the reduced model obtained by the state residualization based MOR technique.

4.1 Review of the State Residualization Based Model Order Reduction in [16]

A power system can be modelled as a nonlinear differential-algebraic system of equations (DAE) as (20).

$$\begin{cases} \frac{dx_d}{dt} = f(x_d, x_a, u) \\ 0 = g(x_d, x_a, u) \\ y = h(x_d, x_a, u) \end{cases}, \tag{20}$$

where $x_d \in \mathbb{R}^{N_d}, x_a \in \mathbb{R}^{N_a}, u \in \mathbb{R}^p, y \in \mathbb{R}^q$, x_d, x_a, u and y represent the algebraic input and output variables, and N_d, N_a, p and q are the related orders.

Residualisation of a state variable consists of changing the state variable into an algebraic variable by neglecting its derivative in the associated differential equation, transforming it into an algebraic equation [21]. It represents a well-known process applied in the phasor approximation to state variables modelling power lines, and used by most of transient simulation programs [22].

The reduced system obtained by state residualisation can be written as in (21).

$$\begin{aligned} E\frac{dx_d}{dt} &= f(x_d, x_a, u) \\ 0 &= g(x_d, x_a, u) \\ y &= h(x_d, x_a, u) \\ E &= diag(\delta_i), \delta_i = \{0,1\}, \forall i \end{aligned} \quad , \qquad (21)$$

where $x_d \in \mathbb{R}^{N_d}, x_a \in \mathbb{R}^{N_a}, u \in \mathbb{R}^p, y \in \mathbb{R}^q$, $E \in \mathbb{R}^{N_d \times N_d}$. The diagonal matrix E is called the residualisation matrix, consisting of 1 or 0 on its diagonal. Each diagonal element $E(i,i)$ indicates whether the state variable $x_d(i)$ is residualised or not. If $E(i,i) = 0$, the state variable $x_d(i)$ is residualised, and otherwise $E(i,i) = 1$. The size of the reduced system is given by $tr(E)$.

The objective of state residualisation is to choose E, giving a trade-off between the order of the reduced model and the expected modelling error.

It is seen that the variables and parameters of the full and reduced models are exactly the same, which ensures that the steady state values of the full and reduced models are the same, as they are computed with the same system. It is also straightforward to directly consider the reduced system for analysis, or tuning and designing of controllers. Finally, state residualisation can be implemented in classical DAE solvers, as it involves substituting some derivative terms by 0.

A method to achieve state residualisation, consisting of state categorisation (based on participation factors calculation, and grouping states and eigenvalues), and modal state residualisation (to preserve some poles according to a given norm), as proposed by [16], is summarized in Fig. 6(a)(b). Details for the two processes are not described here but can be found in [16, 23].

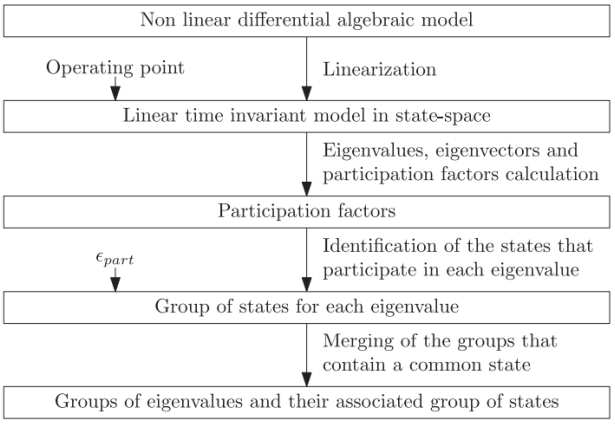

(a)

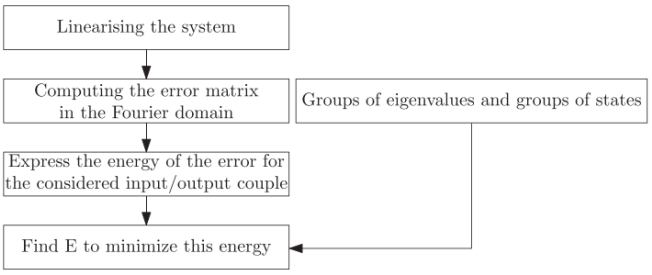

(b)

Fig. 6 Synoptic describing the state categorisation [16] (a), and the modal state residualisation [16] (b).

4.2 Application of the MOR Technique in [16]

Case 1 is considered, and the MOR method in [16] is applied to the system to determine the residualisation matrix E in (21). The input that is considered is the impedance modelling the short-circuit. With a well chosen ϵ_{part} as 0.75 for faults, 12 groups of state variables and eigenvalues are formed, which leads to 2^{16} possible E matrix (i.e. 2^{16} possible reduced models). To save time, genetic algorithm [24] is used here to obtain E.

The output active power of the GFM is observed to form the energy error as the optimal objective function. The desired size is chosen as 8, which is double the order of traditional phasor model for transient stability analysis.

The reserved state variables of the reduced model are shown in Table 2. Based on Table 2, the detailed differential and algebraic equations for the GFM are given as (22)-(25).

$$P = v_{od} i_{od} + v_{oq} i_{oq}, \qquad (22.a)$$

$$\frac{dp_m}{dt} + \omega_c p_m = \omega_c P. \qquad (22.b)$$

$$\omega_{vsm} = \omega_0 + m_p(P^* - p_m), \qquad (23.a)$$

$$\frac{1}{\omega_b}\frac{d\delta_{vsm}}{dt} = \omega_{vsm} - \omega_0. \qquad (23.b)$$

$$v_{od} = V^* - \Delta v_{VId}, \qquad (24.a)$$

$$v_{oq} = -\Delta v_{VIq}. \qquad (24.b)$$

$$\Delta v_{VId} = R_{VI} i_{cd} - X_{VI} i_{cq}, \qquad (25.a)$$

$$\Delta v_{VIq} = R_{VI} i_{cq} + X_{VI} i_{cd}, \qquad (25.b)$$

$$R_{VI} = K_{VI}\, max(0, i_c - I_{nom}), \qquad (25.c)$$

$$X_{VI} = K_{X/R} R_{VI}, \qquad (25.d)$$

$$i_c = \sqrt{i_{cd}^2 + i_{cq}^2}. \qquad (25.e)$$

$$i_{cd} = i_{od} - \omega_{vsm} C_f v_{oq}, \qquad (25.f)$$

$$i_{cq} = i_{oq} + \omega_{vsm} C_f v_{od}. \qquad (25.g)$$

Based on Table 2, the detailed differential and algebraic equations for the SG are given as (26)-(31), where e_d, e_q are d- and q-axis terminal voltage, e_{fd} is the field voltage, ψ_d and ψ_q are d- and q-axis stator flux linkage, ψ_{fd} is the rotor field flux linkage, ψ_{1d}, ψ_{1q} and ψ_{2q} are d- and q-axis rotor

amortisseur flux linkage, i_d, i_q, i_{1d}, i_{1q} and i_{2q} are the related current to the flux linkage, P_m^*, T_e and ω_r are the mechanical power input, electrical torque and rotor speed, V_t^{sg} is the terminal voltage amplitude, E_{fd} is the output of the excitor, EF_{min} and EF_{max} are the minimum and maximum limits of the output of the excitor.

$$e_d = -\psi_q \omega_r - R_a i_d, \tag{26.a}$$

$$e_q = \psi_d \omega_r - R_a i_q. \tag{26.b}$$

$$e_{fd} = \frac{1}{\omega_b}\frac{d\psi_{fd}}{dt} + R_{fd} i_{fd}, \tag{27.a}$$

$$0 = \frac{1}{\omega_b}\frac{d\psi_{1d}}{dt} + R_{1d} i_{1d}, \tag{27.b}$$

$$0 = \frac{1}{\omega_b}\frac{d\psi_{1q}}{dt} + R_{1q} i_{1q}, \tag{27.c}$$

$$0 = \frac{1}{\omega_b}\frac{d\psi_{2q}}{dt} + R_{2q} i_{2q}. \tag{27.d}$$

$$\psi_d = -(L_d + L_{tr}) i_d + L_{ad} i_{fd} + L_{ad} i_{1d}, \tag{28.a}$$

$$\psi_d = -\left(L_q + L_{tr}\right) i_q + L_{aq} i_{1q} + L_{aq} i_{2q}. \tag{28.b}$$

$$\psi_{fd} = L_{ffd} i_{fd} + L_{f1d} i_{1d} - L_{ad} i_d, \tag{29.a}$$

$$\psi_{1d} = L_{f1d} i_{1d} + L_{11d} i_{1d} - L_{ad} i_d, \tag{29.b}$$

$$\psi_{1q} = L_{11q} i_{1q} + L_{aq} i_{2q} - L_{aq} i_q, \tag{29.c}$$

$$\psi_{2q} = L_{aq} i_{1q} + L_{22q} i_{2q} - L_{aq} i_q. \tag{29.d}$$

$$T_e = \psi_d i_q - \psi_q i_d, \tag{30.a}$$

$$2H^{SG}\frac{d\omega_r}{dt} = \frac{P_m^*}{\omega_r} - T_e - K_D^{SG}(\omega_r - \omega_0), \tag{30.b}$$

$$\frac{1}{\omega_b}\frac{d\delta_{sg}}{dt} = \omega_r - \omega_0. \tag{30.c}$$

$$V_t^{sg} = \sqrt{e_d^2 + e_q^2}, \tag{31.a}$$

$$E_{fd} = K_A\left(V_{ref} - V_t^{sg}\right), \tag{31.b}$$

$$EF_{min} \le E_{fd} \le EF_{max}, \tag{31.c}$$

$$e_{fd} = \frac{R_{fd}}{L_{ad}} E_{fd}. \tag{31.d}$$

Table 2 Reserved state variables after using the model order reduction method in [16]

Device	States kept	Description
GFM	δ_{vsm}, ω_{vsm}	The output voltage angle and angular speed of the P/f droop control loop
SG	δ_{sg}, ω_r	Rotor angle and angular speed
	ψ_{fd}, ψ_{1d}	Rotor field and a d-axis amortisseur flux linkage
	ψ_{1q}, ψ_{2q}	2 rotor q-axis amortisseur flux linkage

4.3 Validation of the Obtained Reduced Model

Case 3: Case 1 is re-simulated, but only with the differential state variables shown in Table 2, others turned into algebraic variables. This reduced model is obtained by the adopted residualisation based MOR technique from [16].

Case 4: The settings are the same as Case 3, but the SG is further reduced by turning the states ψ_{1d}, ψ_{1q} and ψ_{2q} to algebraic variables.

Case 5: The settings are the same as Case 4, but the SG is further reduced by turning ψ_{fd} to algebraic variable. This is termed as "modified" classic model. "modified" is used because constant excitation voltage is not used, but the output of the excitor is proportional to the terminal voltage, with the state for the low-pass filter is turned into algebraic variable.

Fig. 7 compares the simulation results of Cases 1, 3 – 5. Fig. 7(a) shows that the GFM active power output in the reduced model under Case 3 have the same waveform as that in the full EMT model under Case 1, with only a delay ~30 ms, which is, however, not critical for respecting converter integrity. On contrast, the waveforms of the GFM active power output under Cases 4 and 5 are very different from the full EMT model.

Fig. 7(c)(d) show that the angular speed of the GFM and SG during the fault under Case 3 are the same as under Case 4, which indicates the same voltage angle difference between the GFM and SG under the two cases. However, Fig. 7(a) shows that the active power output of the GFM under Case 4 is different from Case 3, which is less low and negative. This illustrates that the dynamics of the SG rotor amortisseur flux linkage have negative impact on the postfault active power output of the GFM, making it lower, since the only difference between Cases 3 and 4 is that the dynamics of the SG rotor amortisseur flux linkage are still kept in Case 3. This can be explained as physically SG rotor amortisseur flux linkage is trying to prevent the change of the rotor speed of the SG.

Fig. 7(b) shows that during the fault the SG active power under Case 5 is higher than that under Case 4 (which is due to higher field current in Case 5). This leads to the reduction of the angle difference between the GFM and SG mitigated at the time point of the fault clearance (Fig. 7(e)), since in the SG rotor speed under Case 5 is lower than that under Case 4 (Fig. 7(d)) and the GFM angular speed is not changed under the two cases (Fig. 7(c)). As the angle difference between the GFM and SG affects the GFM postfault power output, this mitigated reduction of the angle difference between the GFM and SG in Case 5 leads to higher active power output of the GFM comparing to Case 4 (Fig. 7(a)).

Fig. 7(e) shows that the converter's current is limited by the VI current limiting control in the reduced models under Cases 3-5. Comparing (24)(25) with (4)(6), it can be seen that, in theory, the MOR method does not modify the VI current limiting control, since it only residualises the state variables.

Fig. 8 compares the poles of the linearised full EMT model and the linearised reduced models under Cases 3 and 5. Table 3 shows the participation factor of the rotor field and amortisseur flux linkage state variables in the most participated eigenvalues. In Fig. 8(b) and Table 3, it can be seen that the eigenvalues $\lambda_{3,4}$ and λ_5 are represented in the reduced model under Case 3, but not represented in the "modified" classic model under Case 5. This eigenanalysis further confirms the above time domain simulation results in Fig. 7 that the reduced model by the adopted MOR technique is more relevant for the system for fault events than the classic model. Specifically, the dynamics of the SG rotor field and amortisseur flux linkage should also be kept along with that of the SG angle and angular speed.

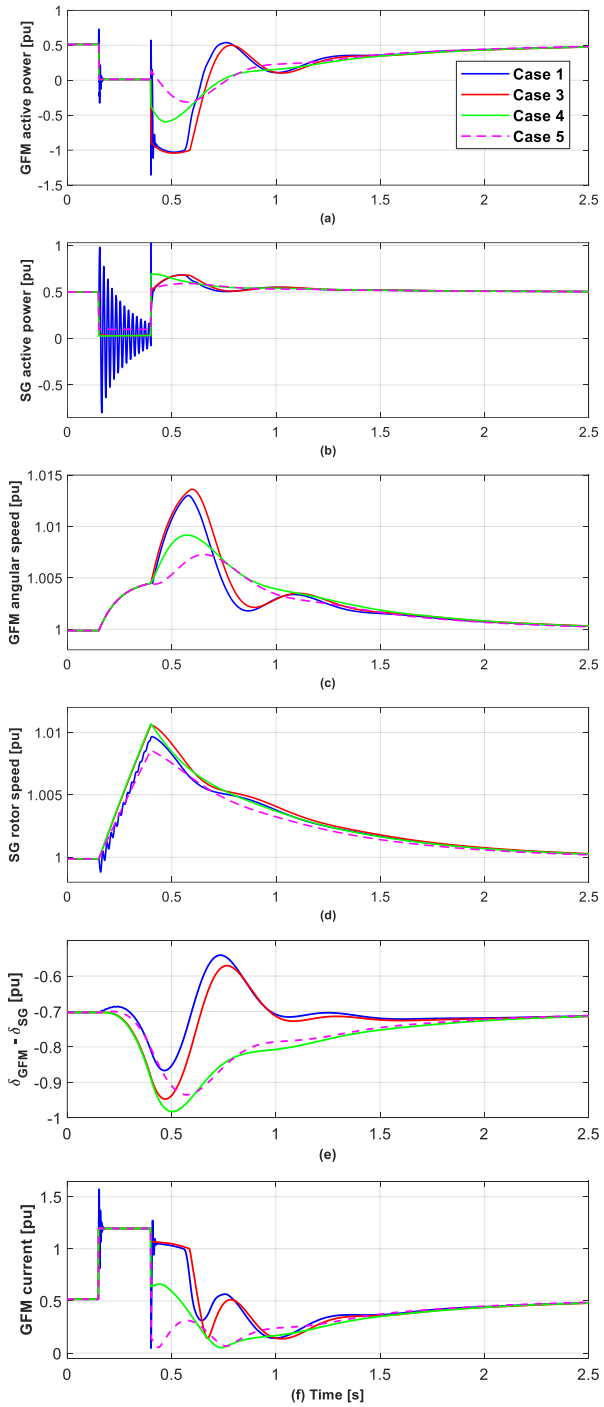

Fig. 7 Results of Cases 1, 3 and 4. (a)(b) The active power output of the GFM and SG, (c)(d) (virtual) angular speed of the GFM and SG, (e) the voltage angle difference between the GFM and SG, and (f) the GFM converter current.

Table 3 SG rotor flux linkage participation factor in the most relevant modes

States	$\lambda_{1,2} = -2.3 \pm j0.1$	$\lambda_{3,4} = -16.7 \pm j12.1$	$\lambda_5 = -25.8$
ψ_{fd}	0.0193	0.4507	0.0090
ψ_{1d}	0.0003	0.3414	0.1099
ψ_{1q}	0.3319	0.0166	0.1817
ψ_{2q}	0.1134	0.0341	0.6328

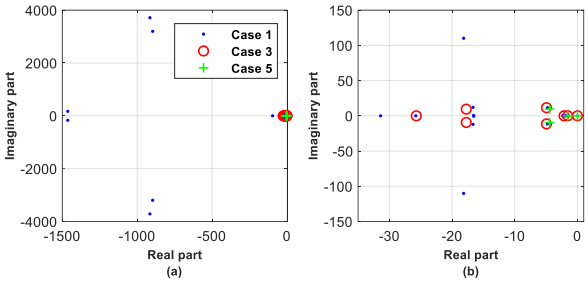

Fig. 8 (a) Poles of the linearised full EMT and reduced models under Cases 3 and 5, and (b) zoomed figure.

5 Transient Stability Analysis and Modelling Simplification for Systems with Only Grid-Forming Converters as Voltage Sources

In previous section, a reduced model for the system with a GFM and SG is obtained, where the reserved states are the angle and angular speed of both GFM and SG together with the SG rotor field and amortisseur flux linkage. In this section, the target is to validate whether a system with only GFMs as voltage sources can reduced with only the angle and angular speed of the GFMs as the reserved states.

Case 5: The settings are the same as Case 1, but G1 and G2 are both GFMs. G1 inertia and damping are $m_p = 0.01$ pu and $\omega_c = 10$ rad/s, and for G2 are $m_p = 0.2$ pu and $\omega_c = 0.5$ rad/s. Note that the capacity ratio of G1 over G2 is 9.

Case 6: The settings are the same as Case 5, but all the differential variables are turned into algebraic ones except the states angle and angular speed, δ_{vsm} and ω_r, of the GFMs.

The simulation results of Cases 5 and 6 are shown in Fig. 9. Under Case 5, Fig. 9(b) shows that the angular speed of G1 is smaller than that of G2 during the fault, and hence the angle difference between G1 and G2 at the time point of the fault clearance is reduced. Thus, the active power output of G1 is negative after the fault is cleared (Fig. 9(a)) (Note that G1 is transient unstable according to the traditional definition). Comparing Fig. 3(a)(b) with Fig. 9(a)(b), it is seen that the active power output and angular speed of G1 and G2 in Case 5 have very similar shape as in Case 1. This is due to the same inertia and damping for G1 and G2 in both cases. Hence, consistent inertia and damping for all GFMs are recommended in future power systems or in local areas.

It is also seen that the dynamics of G1 and G2 under Case 6 are well matched with that under Case 5. This demonstrates that by only keeping the state variables of the angle and angular speed of GFMs (note that other relevant algebraic equations such as virtual impedance current limiting control still exist), the reduced model is feasible for transient stability analysis of systems with only GFMs as voltage sources. This claim is also applicable for other types of GFMs, such as dispatchable virtual oscillator (dVOC) [25]. Due to space limitations, the simulation results are not shown here.

Case 7: The settings are the same as Case 5, but the inertia and damping for G1 and G2 are swapped, i.e. for G1 $m_p =$

0.2 pu and $\omega_c = 0.5$ rad/s, and for G2 $m_p = 0.01$ pu and $\omega_c = 10$ rad.s. The capacity ratio of G1 over G2 is still 9.

Case 8: The settings are the same as Case 7, but all differential variables are turned into algebraic ones except the states angle and angular speed, δ_{vsm} and ω_r, of the GFMs.

The simulation results of Cases 7 and 8 are shown in Fig. 10. Under Case 7, Fig. 10(b) shows that G1 angular speed is larger than that of G2 during the fault, and hence the G1 and G2 angle difference at the time point of the fault clearance is increased. Thus, G1 active power output is positive after the fault is cleared (note that G1 is transient stable according to the traditional definition), as seen in Fig. 10(a).

Fig. 10(a) shows that the active power output of G1 oscillates heavily. The eignanalysis results in Fig. 11 show that in Case 7 appears a pair of oscillating modes with small damping and being close to the imaginary axis, which does not exist in Case 5. The oscillating characteristics again confirm that setting consistent inertia and damping for all GFMs in future power systems is a preferred option.

Fig. 10 also shows that the oscillating characteristics of G1 and G2 under Case 7 are well represented in Case 8, which demonstrates that by only keeping the state variables of the angle and angular speed of GFMs is feasible for system transient stability analysis with only GFMs as voltage sources. Other cases with G1 and G2 of the same inertia and damping further confirm this conclusion. The simulation results (not shown here) show that the two GFMs immediately recover to pre-fault active power after a fault is cleared, and such characteristic still exist when the inertia, damping and the type of the GFMs (e.g. droop control based GFM, dVOC, or mixed types) are changed.

6 Conclusion

The transient stability of systems consisting of GFMs and SGs under large faults is studied. It finds out that even when the SGs and GFMs have the same rotor speeds during a fault when both are set the same inertia and damping coefficients, due to the dynamics of the field flux and amortisseur flux of the SG, the connected GFM with small GFM and SG capacity ratio outputs negative postfault active power. Based on traditional definition, this is synchronization unstable. The negative active power output becomes lower and lasts longer in real applications because typically GFMs have much larger damping coefficients. In current literature, to simplify analysis and control design for large events like faults, existing methods tend to model a GFM in the same form as the classic SG model, which however do not give theoretical basis. This paper adopts a modal analysis- and residualisation- based model order reduction technique (that optimizes the reduced number of state variables of a system depending on the observed variables and considered events), and finds out that while a GFM can be modelled as the classic form for a SG along with the virtual impedance current limiting control, the nearby SG should not be modelled in the classic form, since the dynamics of the rotor field and amortisseur flux linkage should also be included. Finally, this paper finds that for systems with only GFMs as voltage sources, representing GFMs in this classic form (reserving the GFMs angle and angular speed variables along with the virtual impedance current limiting control) is enough for representing the system low-frequency oscillation phenomenon.

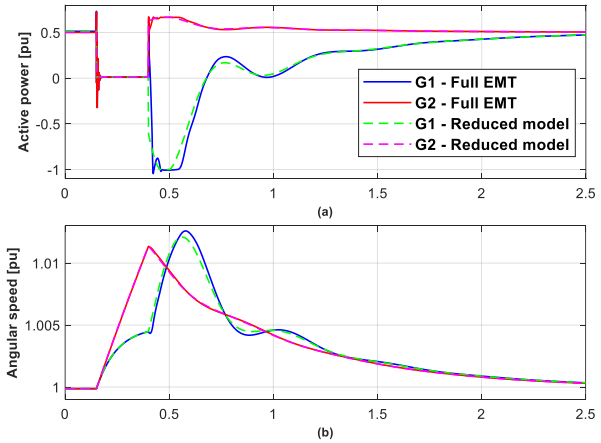

Fig. 9 Comparison simulation results of Cases 5 and 6. (a)-(c) The active power output, virtual angular speeds, and converter current of the G1 and G2.

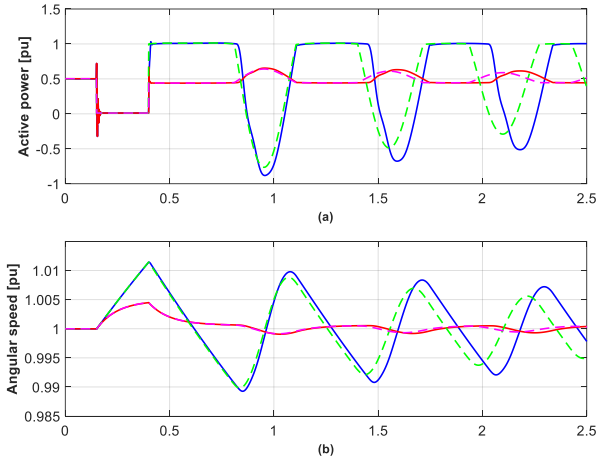

Fig. 10 Comparison simulation results of Cases 7 and 8. (a)-(c) The active power output, virtual angular speeds, and converter current of the G1 and G2. The legends are the same as Fig. 9.

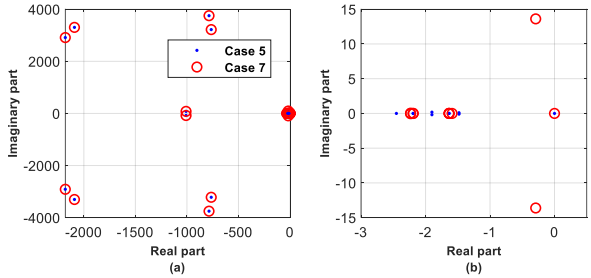

Fig. 11 Eigenvalues comparison of Cases 5 and 7.

7 Acknowledgements

The work has been supported by SEAI (Sustainable Energy Authority of Ireland) under RD&D Award 22/RDD/776.

8 References

[1] Hodge, B.M.S., et al., 'Addressing technical challenges in 100% variable inverter - based renewable energy

power systems', Wiley Interdisciplinary Reviews: Energy and Environment, 2020, 9(5), p. e376.
[2] Rocabert, J., Luna, A., Blaabjerg, F. and Rodriguez, P.: 'Control of power converters in AC microgrids', IEEE Trans. Power Electron., 2012, 27(11), pp. 4734-4749.
[3] M. Yu et al.: 'Instantaneous penetration level limits of non‐synchronous devices in the British power system', IET Renew. Power Gener., 2017, 11(8), pp. 1211-1217.
[4] Zhao, X., Thakurta, P.G., Flynn, D.: 'Grid-forming requirements based on stability assessment for 100% converter-based Irish power system', IET Renew. Power Gener., 2022, 16, pp. 447–458.
[5] Infineon, 'AN2011-05 Industrial IGBT Modules Explanation of Technical Information', November 2015.
[6] Huang, L., Xin, H., Wang, Z., Zhang, L., Wu, K. and Hu, J.: 'Transient stability analysis and control design of droop-controlled voltage source converters considering current limitation', IEEE Trans. Smart Grid, 2017, 10(1), pp. 578-591.
[7] Qoria, T., et al.: 'Critical clearing time determination and enhancement of grid-forming converters embedding virtual impedance as current limitation algorithm', IEEE Trans. Emerg. Sel. Topics Power Electron., 2019, 8(2), pp. 1050-1061.
[8] Rokrok, E., Qoria, T., Bruyere, A., Francois, B. and Guillaud, X.: 'Transient stability assessment and enhancement of grid-forming converters embedding current reference saturation as current limiting strategy', IEEE Trans. Power Syst., 2021, 37(2), pp. 1519-1531.
[9] Pan, D., Wang, X., Liu, F. and Shi, R.: 'Transient stability of voltage-source converters with grid-forming control: A design-oriented study', IEEE Trans. Emerg. Sel. Topics Power Electron., 2019, 8(2), pp. 1019-1033.
[10] Shuai, Z., Shen, C., Liu, X., Li, Z., Shen, Z.J.: 'Transient angle stability of virtual synchronous generators using Lyapunov's direct method', IEEE Trans. Smart Grid, 2018, 10(4), pp. 4648-4661.
[11] Me, S.P., et al.: 'Transient Stability of Paralleled Virtual Synchronous Generator and Grid-following Inverter', IEEE Trans. Smart Grid, 2023. doi: 10.1109/TSG.2023.3255168
[12] He, X., Pan, S. and Geng, H.: 'Transient stability of hybrid power systems dominated by different types of grid-forming devices', IEEE Trans. Energy Conv., 2021, 37(2), pp. 868-879.
[13] Zhao, X., Flynn, D: 'Freezing grid-forming converter virtual angular speed to enhance transient stability under current reference limiting', IEEE 21st Workshop Control Modeling Power Electronics Aalborg, Denmark, 2020.
[14] Cheng, H., et al.: 'Transient angle stability of paralleled synchronous and virtual synchronous generators in islanded microgrids', IEEE Trans. Power Electron., 2020, 35(8), pp. 8751-8765.
[15] Zhao, X. and Flynn, D.: 'Grid-forming converter angular speed freezing to enhance transient stability in 100% grid-forming and mixed power systems', IFAC-PapersOnLine, 2022, 55(9), pp. 425-430.
[16] Cossart, Q., Colas, F. and Kestelyn, X.: 'A novel event- and non-projection-based approximation technique by state residualization for the model order reduction of power systems with a high renewable energies penetration', IEEE Trans. Power Syst., 2020, 37(4), pp. 3221-3229.
[17] Bottrell, N. and Green, T.C.: 'Comparison of current-limiting strategies during fault ride-through of inverters to prevent latch-up and wind-up', IEEE Trans. Power Electron., 2013, 29(7), pp. 3786-3797.
[18] D'Arco, S., Suul, J.A., Fosso, O.B.: 'Automatic tuning of cascaded controllers for power converters using eigenvalue parametric sensitivities', IEEE Trans. Ind. Appl., 2014, 51, pp. 1743–1753.
[19] Kundur, P.: Power system stability and control. New York: McGraw-Hill, 1994.
[20] Qoria, T., et al.: 'Tuning of cascaded controllers for robust grid-forming voltage source converter', Proc. Power Syst. Comput. Conf., 2018.
[21] Antoulas, A.C.: Approximation of large-scale dynamical systems. SIAM, 2005.
[22] I. J. Pérez-Arriaga, G. C. Verghese, and F. C. Schweppe, 'Selective modal analysis with applications to electric power systems, Part I: Heuristic introduction', IEEE Trans. Power Appar. Syst., 1982, 9, pp. 3117-3125.
[23] Cossart, Q.: 'Outils et méthodes pour l'analyse et la simulation de réseaux de transport 100% électronique de puissance', PhD, Laboratoire d'Electrotechnique et d'Electronique de Puissance (L2EP) de Lille, Hesam Université, Paris, France, 2019.
[24] Lee, K.Y. and El-Sharkawi, M.A.: Modern heuristic optimization techniques: theory and applications to power systems. John Wiley & Sons, 2008.
[25] Seo, G.S., Colombino, M., Subotic, I., Johnson, B., Groß, D. and Dörfler, F.: 'Dispatchable virtual oscillator control for decentralized inverter-dominated power systems: Analysis and experiments', in Proc. IEEE Appl. Power Electron. Conf., Mar. 2019, pp. 561-566.